Nuclear Engineering and Technology 54 (2022) 262–268

Contents lists available at ScienceDirect

Nuclear Engineering and Technology

journal homepage: www.elsevier.com/locate/net

Original article

Neutronic design of pulsed neutron facility (PNF) for PGNAA studies of biological samples

Kyuhak Oh

Department of Nuclear, Plasma Radiological Engineering, University of Illinois, IL, 61801, USA

ARTICLE INFO

Article history:
Received 2 November 2020
Received in revised form
12 July 2021
Accepted 16 July 2021
Available online 21 July 2021

Keywords:
D-T neutron generator
Prompt gamma neutron activation analysis
Trace element
Neutron-induced reactions
Characteristic γ-ray
Shielding and moderation

ABSTRACT

This paper introduces a novel concept of the pulsed neutron facility (PNF) for maximizing the production of the thermal neutrons and its application to medical use based on prompt gamma neutron activation analysis (PGNAA) using Monte Carlo simulations.

The PNF consists of a compact D-T neutron generator, a graphite pile, and a detection system using Cadmium telluride (CdTe) detector arrays. The configuration of fuel pins in the graphite monolith and the design and materials for the moderating layer were studied to optimize the thermal neutron yields. Biological samples – normal and cancerous breast tissues – including chlorine, a trace element, were used to investigate the sensitivity of the characteristic γ-rays by neutron-trace material interactions and the detector responses of multiple particles.

Around 90 % of neutrons emitted from a deuterium-tritium (D-T) neutron generator thermalized as they passed through the graphite stockpile. The thermal neutrons captured the chlorines in the samples, then the characteristic γ-rays with specific energy levels of 6.12, 7.80 and 8.58 MeV were emitted. Since the concentration of chlorine in the cancerous tissue is twice that in the normal tissue, the count ratio of the characteristic γ-rays of the cancerous tissue over the normal tissue is approximately 2.

1. Introduction

In the past, a general neutron generator was usually used only for well-logging for the oil field industry as a replacement for some neutron sources such as AmBe and ^{252}Cf [1]. Along with advantages, application to neutron generators has been extended to a wide range of areas for nuclear, biological, and medical science and engineering as well as security [2].

A facility called the PNF was constructed to study material analysis related to nuclear and biological materials consisting of chemical elements using a D-T compact neutron generator. There had been a TRIGA reactor since the 1960s, and it was shut down in 1998. A graphite-uranium subcritical (GUS) assembly including Al-clad natural uranium annular fuel rods in a reactor-grade graphite matrix had been a part of the TRIGA reactor [3]; recently, a pulsed neutron generator was equipped for more expanded research related to neutrons. Neutrons emitted and thermalized by this facility could be used as a source of the NAA method, which is a non-destructive, rapid, safe, and precise way, for detection and identification of a specific element in chemical, biological, and nuclear samples by the neutron absorption reactions, which create characteristic γ-rays of specific energy level [4–6].

This research provides a useful guideline for the novel disease diagnostic method using PGNAA. Especially, characteristic γ-rays emitted from the interactions of thermalized neutrons with a trace element, chlorine, were investigated and analyzed for breast cancer diagnosis.

2. Model specification

The PNF is a characteristic system for research related to neutron transports and neutron-material interactions. It makes this facility possible to study nuclear material effects related to moderator and fuel, material analysis based on the detection of specific neutrons, or characteristic γ-rays by the interactions of neutrons with matters. Fig. 1 shows the PNF components – Graphite assembly, D-T neutron generator, and detector array - and MCNPX 2D model of the PNF consisting of a fueled graphite monolith and a detection system [7].

The reactor-grade graphite assembly was constructed with channels for Al-clad, natural uranium, annular fuel rods

E-mail address: koh39@illinois.edu.

https://doi.org/10.1016/j.net.2021.07.024

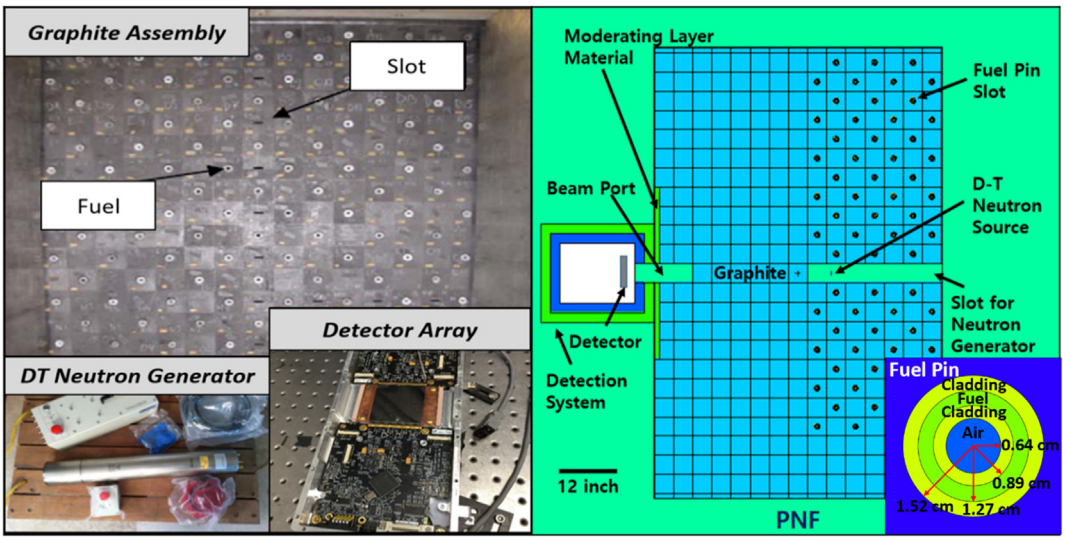

Fig. 1. PNF components (Left) and MCNPX 2D model of the PNF (Right).

incorporating a pulsed D-T neutron generator to produce fast neutrons. Its dimension is 152 × 152 cm^2 with a 193 cm-height surrounded by a 0.1 cm-thick cadmium liner and 0.3 cm-thick aluminum panels. The model of the fuel pin was based on the Savannah River natural uranium hollow slug of TRIGA [3]. This fuel pin is cylindrical, and its height and diameter are 20.83 cm and 1.52 cm, respectively, as shown in Fig. 1. It has a hollow space at the center, and aluminum claddings surround the natural uranium fuel. The MCNPX model presents the optimized PNF geometry with seven fuel pins, which is explained in Section III.

The PNF holds a pulsed neutron generator in a central horizontal beam port at the mid-plane of the graphite monolith. The neutron generator uses D-T fusion reactions, D(T, n)^{4}He, to produce high-energy neutrons. The neutron generator generates isotropically 14.1-MeV neutrons of a yield of 3 × 10^8 particles/second with a peak yield of 5 × 10^8 particles/second. This generator can also regulate neutron pulses with pulse widths between 5 and 1000 μs at a frequency between 250 and 20,000 Hz [8]. The spectra follow the Gaussian distribution curve centered. The graphite assembly moderates the high-energy neutrons produced by the D-T generator and the fuel pins cause a subsequent fission reaction population.

As shown in Fig. 2, the detection system consists of a detector array, a sample, and the appropriate shielding layers. This system detects characteristic γ-rays by thermal neutron capture γ-ray reactions with the sample material. The detector units consist of eight smaller detector subunits, which dimensions are 128 × 128-pixel square. Since each pixel measures 350 μm^2, each detector subunit placed 7 cm away from the center of the sample, has a thin rectangular shape measuring 44.8 × 44.8 × 2.2 mm^3 [9]. Cadmium telluride (CdTe) is chosen as the detector material due to its high spatial resolution, wide bandgap, higher detection efficiency, and good electron transport characteristics at room temperature or higher [10–14]. It could also detect both photon and neutron as well as provide a non-destructive, rapid, safe, and precise way to analyze the elemental contents in chemical, biological, and nuclear samples [15–17]. The sample is located at the center of the detector array for maximizing the detection of characteristic γ-ray signals created by the neutron interactions since the characteristic γ-rays were emitted isotropically. The sample has a cylindrical shape of a 2-cm radius and a 4.48-cm height and its density is 1.02 g/cm^3. The radius was selected with consideration for the beam port size, while the height was chosen in light of one side length of the detector. Combined shielding layers play a role in decreasing background particles – γ-rays and neutrons. The shielding layers surrounding the box-shaped inner space measured to 32 × 32 × 40 cm^3 consist of a 5 cm-thick of high-density polyethylene (HDPE, outer), a 5 cm-thick lead, and a 1 mm-thick cadmium (inner). The HDPE layer decelerates high-energy background neutrons; then the thermalized background neutrons could be absorbed in the cadmium layer. The lead layer shields background γ-rays.

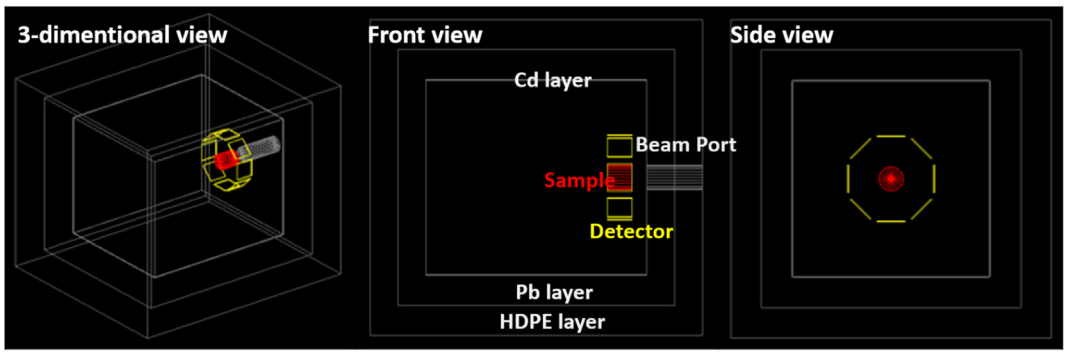

Fig. 2. Diagrams of the detection system.

For safety, the PNF is surrounded by a 60.96 to 91.44 cm-thickness shielding barrier made of ordinary concrete to reduce dose leakages [17].

3. Beam and sample characteristic

Because of complicated geometries, the Monte Carlo simulation requires a significant amount of time to reach a final result. Two phases were applied to reduce the unnecessary running time. The first phase is the MCNPX simulation for the optimized PNF geometry using the ENDF/B-VII.1 cross-section library [18]. The second phase sets the detector responses of particle interactions within sample materials by the GATE simulation employing high precision models such as G4NeutronHPInelastic and G4NeutronHPCapture for the cross-section data [19]. Based on the optimal PNF geometry discussed in the previous section, inwardly traveling flux at the innermost surfaces of the detection system calculated by the MCNPX was set as the source for the GATE simulation in the second phase.

The optimized PNF was designed for the maximized production of primary thermal neutrons and the minimized yield of background neutrons at the innermost surfaces of the detection system. The neutrons produced by the neutron generator at the center of the PNF were passing through the fueled graphite monolith, the moderating layer, and the shielding layers of the detection system; then, the surface neutron fiux reached the innermost surfaces of the detection system was calculated considering of various factors such as the configuration of fuel pins and the design and type of materials for the moderating layer. Both thermalized and optimized factors were defined to determine the thermalized level of the source neutrons and the optimization level of the system. To assess the optimized level of the system, three parameters were considered: 1) the ratio of thermalized neutrons on the innermost surface of the beam port of the detection system, 2) the flux of thermal neutrons on the innermost surface of the beam port of the detection system, and 3) the energy range of the total neutron flux on the innermost surfaces of the detection chamber, excluding neutrons passing through the beam port.

Since only thermal neutrons passing through the beam port lead to foreground radiative capture events, the maximized thermal neutron flux is a significant barometer. The thermalization factor, L_{TF}, presents a ratio of the number of thermal neutrons to the number of total neutrons passing through the beam port and is defined by:

$$L_{TF} = \frac{\varnothing_{Thermal}}{\varnothing_{Tot}} = \frac{\int_{Thermal} \phi(E)dE}{\int_{Total} \phi(E)dE} = 1 - \frac{1}{R_{cd}}, \quad (1)$$

where R_{cd}, cadmium ratio, is the ratio of the number of all energies of neutrons getting the detector to the number of neutrons when the detector is covered with the cadmium, ϕ_{Tot} is all energies of neutron flux on the inner surface of the beam port of the detection system, $\phi_{Thermal}$ is thermal neutron flux with the energy of 0.0025 eV or below on the inner surface of the beam port of the detection system, and $\phi(E)$ is the energy-dependent flux. With background neutrons passing through the innermost surfaces of the detection chamber, the optimized factor is further defined by:

$$L_{OF} = L_{TF} \times \frac{\varnothing_{Thermal}}{\varnothing_{Background}} = L_{TF} \times \frac{\int_{Thermal} \phi(E)dE}{\int_{Total} \phi(E)dE}, \quad (2)$$

where $\phi_{Background}$ is all energies of the neutron flux on the inner surfaces of the detection chamber, except for the neutrons traversing the beam port. Fig. 2 shows a diagram of the detection system for the definition of the optimized geometry. Multiple calculations of the neutron flux of the innermost surfaces of the detection system were performed by the MCNPX simulations using the F2 tally option for the averaged scalar flux of the particles over a surface [7], then the thermalization and the optimization factors were determined in consideration of the number of fuel pin columns removed and effect of moderating layer.

Fission reaction increases neutron production; then, thermalized neutrons react with the uranium fuel pins, increasing the neutron production. The fuel arrangement of the PNF, therefore, is a significant factor considered. MCNPX simulations based on different configurations of fuel pins, ranging from no fuel to the fully-fueled state, were performed multiple times, then the thermalization factor and the optimization factor were calculated. Fig. 3 represents the calculated thermalization factor, L_{TF}, and optimization factor, L_{OF}, versus the number of fuel pins removed. The thermalization factor increases sharply then becomes stable when six columns of fuel pins closest to the detection system are removed. Because the ratio of neutrons produced by fission reactions with a range of energies between 1 and 10 MeV [20] decreases as the columns of fuel pins close to the detection system are removed. This process also causes to decrease the background neutron flux. The optimization factor curve also shows a similar tendency with the thermalization factor curve, reaching a maximum value when eight columns of fuel pins are removed. After this maximum, the optimization factor decreases as more fuel pin columns are removed due to the thermalization of the fission neutrons by the fuel pins of the PNF at the innermost surface of the beam port of the detection system. With more fuel pins, the fast and epithermal neutrons compared to the thermal neutrons at the innermost surface of the beam port increase due to the short distance between the fuel pins and the innermost surface. Vice versa, the fast and epithermal neutrons rarely reach the innermost surface of the beam port; then, the ratio of the thermal neutrons to the total yielded neutrons at the innermost surface of the beam port is highest, but the actual number of the thermal neutrons is smallest.

Types of materials for the moderating layer were investigated for increasing the thermalized neutrons at the innermost surface of

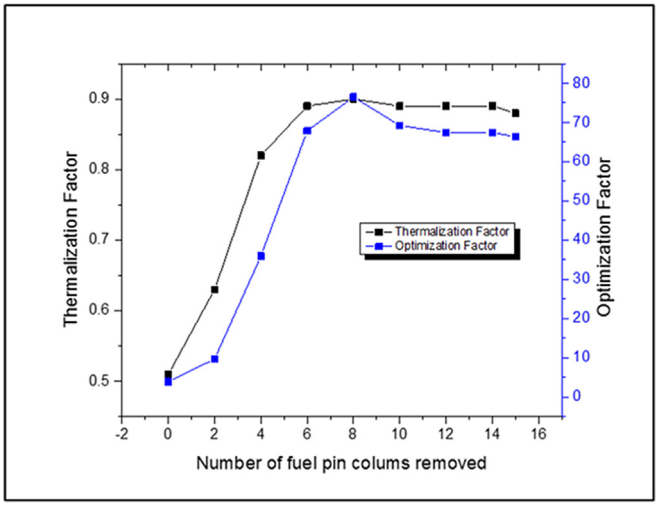

Fig. 3. L_{TF} and L_{OF} versus the number of fuel pin columns removed (See Fig. 3 for geometry).

the beam port of the detection system and decreasing the background neutrons. For this, a moderating layer was defined and located in the graphite monolith and at the border of the detection system, as shown in Fig. 1. The materials for the moderating layer considered were boron carbide, borated polyethylene, water, heavy water, polyethylene, deuterated polyethylene, and beryllium, which are usually used as the shielding and moderating materials. The different materials for the moderating layer were simulated to further determine the optimization factor and the thermalization factor. Monte Carlo simulations using different thicknesses – 0, 2.54, 5.08, and 10.16 cm - were performed to determine the optimal thickness of the material for the moderating layer, and a 2.54-cm thick layer was selected as the optimum thickness. The results of these simulations are represented in Table 1. Both diffusion length and Fermi age are principal factors deciding if a material has a good moderating characteristic. The diffusion length corresponds to the average distance traversed by the particle from birth to the absorption, while Fermi age is defined as the mean square distance when slowing down of the fission neutrons. Using polyethylene compared to other materials, the optimization factor reached the maximum because of the smallest Fermi age and diffusion length as opposed to the other materials. For example, the diffusion length and Fermi age of the polyethylene are 2.12 cm and 19.8 cm^2, respectively, while those of the water are 2.85 cm and 27.0 cm^2 [21–23]. The fast and epithermal neutrons are moderated to thermal neutrons as they pass through the moderating layer and are absorbed by the cadmium liner of the PNF; then, fewer background neutrons are emitted when using the polyethylene compared to the other materials. This is due to the hydrogen atoms in polyethylene causing multiple collisions with fast and epithermal neutrons; thus, both neutrons lost energy and were moderated to thermal energy level. The thickness of the moderating layer is also investigated in the case of polyethylene.

As shown in the left picture of Fig. 4, the thermalized neutrons at the innermost surfaces of the beam port were defined as the primary neutrons since these neutrons were needed to interact with the sample material. Except for these neutrons, all other particles including γ-rays were defined as the background particles. The right picture of Fig. 4 represents the energy spectrum of the primary neutrons at the innermost surface of the beam port of the detection system in a 3-D parameter space of energy and angular distribution. It shows over 90% of the primary neutrons are thermalized based on the MCNPX result. This large percentage of thermal neutrons is due to the PNF geometry, which was optimized for beam specification with the best arrangement of the fuel fins and the moderating layer material. The number of thermal neutrons tends to decrease dramatically with an increasing angle. The thermal neutrons traversing the beam port tended to go straight without any interactions, while the other thermal neutrons scattered by the beam port wall had lost their energies. In other words, the beam port influences the beam intensity and distribution angle, which, in turn, affects the thermal neutron production. At the innermost surface of the beam port, most thermal neutrons with a small portion of fast and epithermal neutrons were passing through with a smaller angular distribution. The fast and epithermal neutrons being able to strike the innermost surface of the beam port did so without any significant interactions with the materials for the moderating and shielding layers.

Table 1
Thermalization factors and optimization factors of different materials for moderating layer.

Material for moderating layer	L_{TF}	L_{OF}
Boron Carbide	0.88	151
5 % Borated Polyethylene	0.87	136
30 % Borated Polyethylene	0.87	136
Water	0.90	174
Heavy Water	0.88	145
Polyethylene	0.90	187
Deuterated Polyethylene (CD_2)	0.88	129
Beryllium	0.88	151

Human breast tissues were modeled as biological samples – both cancerous and normal tissues. As shown in Table 2, both samples are mainly composed of the same chemical elements but have relatively different concentrations. Some trace elements, such as sodium (Na), chlorine (Cl), potassium (K), and calcium (Ca), differ significantly between normal and cancerous breast tissues because cancer influences the physiological functions of the human body, which results in the variation of the concentrations of the trace elements between the malignant and normal tissues. This research focuses on one of the trace elements, chlorine, since it has a strong signal of the characteristic γ-rays by thermal neutron capture reactions and is relatively abundant in the human body [24,25].

4. Neutron and γ-ray interactions with the sample

Both primary neutrons and background particles contribute to the interactions with sample and detector materials. The left picture of Fig. 5 shows all neutron interactions with the sample and the detector considered. Primary neutrons have a much higher probability of interacting with the sample than the background neutrons. (1) ~ (3) indicate the γ-ray interactions with the detector after neutron capture reactions by the sample. Only γ-rays from (3) could be used as detection signals as a result of neutron capture reactions for the specific trace element, chlorine, of the sample. (4) ~ (9) are categorized as the background signals since the neutrons interact with the detector directly; then, the capture γ-rays are produced and interact with the detector. (4) ~ (6) show the scattered neutrons by the sample; then, they are captured by the detector. The neutrons of (7) ~ (9) are captured directly by the detector without any interactions with the sample. Thus, the signal peak relies on the photoelectrons in the detector, and the photoelectric effect caused by the γ-rays created from the neutron capture reactions with the sample. Except for these electrons, all created particles could be defined as the background particles. As shown in the left picture of Fig. 5, γ-rays created by the interactions with shielding materials could be getting the detector with or without interactions with the sample. All γ-rays are categorized as background particles. (1) ~ (4) represent the γ-ray interactions in the detector after scattering in the sample. In the cases of (5) ~ (9), the γ-rays interact directly with the detector without any interactions with the sample.

5. Results and discussion

The γ-ray energy spectra for both tumorous and normal tissues of the breast as well as the spectrum without any sample were obtained, as shown in Fig. 6. The primary neutrons with backgrounds particles were generated, and the CdTe detector was used to derive the γ-ray signals by the neutron interactions with the sample. The γ-ray spectrum with no sample was used to study the contributions of the trace element, chlorine, to the signal peaks. Comparing to the γ-ray energy spectrum with no sample, the contribution of some elements such as hydrogen, chlorine, and nitrogen in the sample could be explained. The peaks at 2.23 MeV (#2), 6.12 MeV (#9), 7.80 MeV (#10), 8.58 MeV (#11), and 10.84 MeV (#13) were thought to have originated from the sample. Especially, the three peaks at 6.12 MeV (#9), 7.80 MeV (#10), 8.58 MeV (#11) were involved in the trace element, chlorine. The rest of the peaks came from neutron interaction with the shielding materials of the detection system and the self-absorption of the

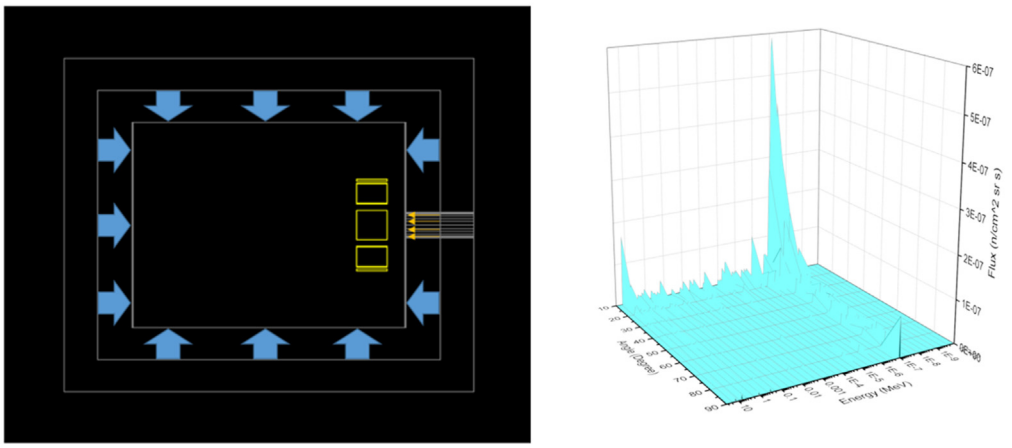

Fig. 4. Generating primary neutrons and background particles at the inner surfaces (left) and energy spectrum of primary neutrons at the innermost surface of the beam port of the detection system (right). The yellow arrows represent the primary neutrons while the blue arrows represent the background particles. (For interpretation of the references to colour in this figure legend, the reader is referred to the Web version of this article.)

Table 2
The element concentrations for normal and tumor breast tissue [26].

Element	Normal Tissue		Tumor Tissue	
	Mass Fraction	Mass (mg)	Mass Fraction	Mass (mg)
H	0.105407	6052.83	0.103909	5966.82
C	0.330143	18957.91	0.325452	18688.52
N	0.029832	1713.06	0.029408	1688.72
O	0.524053	30092.83	0.516606	29665.21
Na	0.003969	227.91	0.007777	446.58
Al	0.000014	0.82	0.000022	1.27
Cl	0.004227	242.73	0.008359	480.00
K	0.001913	109.85	0.007628	438.02
Ca	0.000177	10.19	0.000438	25.17
Mn	0.000001	0.05	0.000001	0.07
Fe	0.000210	12.04	0.000306	17.54
Co	0.000000	0.03	0.000001	0.04
Zn	0.000025	1.44	0.000044	2.54
Br	0.000015	0.87	0.000025	1.46
Rb	0.000013	0.74	0.000023	1.30

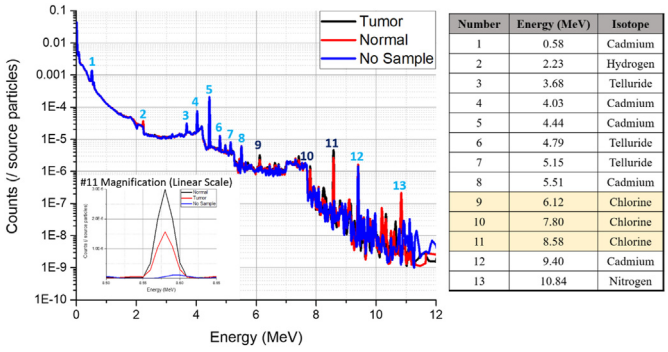

Number	Energy (MeV)	Isotope
1	0.58	Cadmium
2	2.23	Hydrogen
3	3.68	Telluride
4	4.03	Cadmium
5	4.44	Cadmium
6	4.79	Telluride
7	5.15	Telluride
8	5.51	Cadmium
9	6.12	Chlorine
10	7.80	Chlorine
11	8.58	Chlorine
12	9.40	Cadmium
13	10.84	Nitrogen

Fig. 6. The γ-ray energy spectra using primary neutrons and background particles with the CdTe detector for both tumor and normal tissues of the breast as well as no sample.

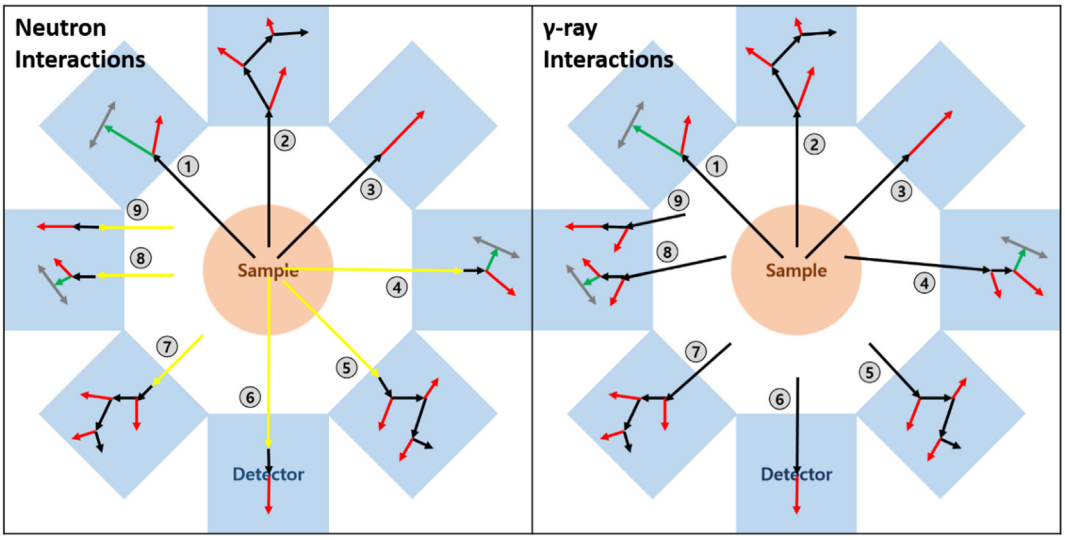

Fig. 5. Diagrams of the neutron (left) and γ-ray (right) interactions with sample and detector materials (Yellow: neutron, Black: γ-ray, Red: electron, Green: positron, Gray: annihilation γ-ray). (For interpretation of the references to colour in this figure legend, the reader is referred to the Web version of this article.)

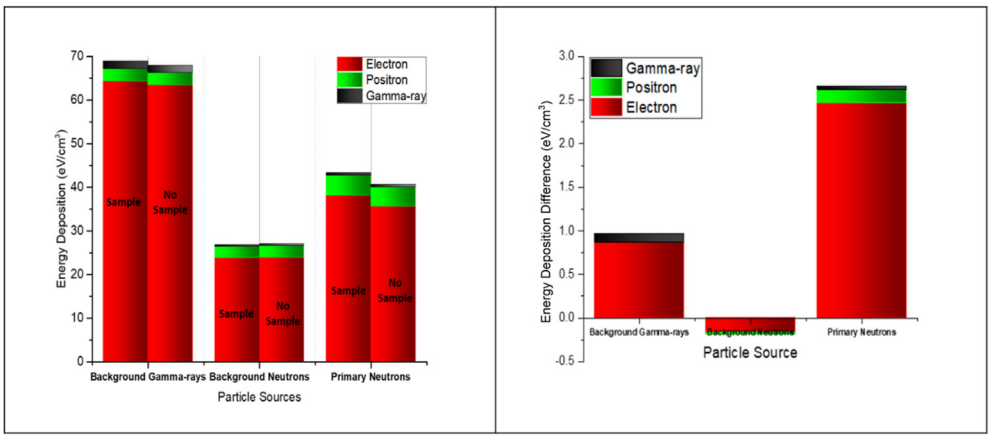

Fig. 7. Energy deposition by individual particles with and without the sample (left) and energy deposition difference between with and without the sample (right). The energy deposition differences for each particle represent the subtractions of the deposited energy with sample by the deposited energy without sample.

neutrons in the detector material [27].

When comparing both spectra for tumorous and normal tissues, there is a gap in the count area at those peaks made up of the chlorine. These peaks came from the neutron capture γ-ray emission reaction with chlorine in the sample of the breast tissue. Since chlorine has a large cross-section for neutron capture γ-ray reaction, the chlorine peaks are more clearly discriminated than for those of the other trace elements [26,28]. As shown in Table 2, the concentrations of sodium and potassium are as high as that of chlorine. Those peaks for both elements could not be observed in the spectra, however, due to their low neutron capture cross-section. It is very difficult to observe the signal peaks of chlorine in the low energy range because of the high background γ-ray signals by interactions with the materials for the shielding and moderating layers. The background γ-ray signals tend to decrease as the energy increases. Therefore, the peaks in the range of high energy are easy to be differentiated than the peaks in the low energy range due to low background signals. In this case, contributions to the signature peaks at 6.12, 7.80, and 8.58 MeV are dominated by the interactions of the primary neutrons.

There should be multiple interactions by neutrons and γ-rays in the detector, as shown in Fig. 5. The secondary particles created by the photoelectric interactions with the detector contribute to the signals for the characteristic γ-ray detection. Since the deposited energy by primary γ-rays is equal to the energy of the ionized secondary particles, the deposited energy of the secondary particles including electrons, positrons, and γ-rays (annihilation) could be calculated. Particle sources were classified in the primary neutrons, background neutrons, and background γ-rays. Using GATE simulations, the deposited energy by individual particles – γ-ray, positron, and electron – was calculated. Therefore, the energy deposition contribution by each particle source was analyzed in consideration of each secondary particle created by source particle interactions with and without the sample.

The left picture of Fig. 7 shows the deposited energies by the individual particles with and without the sample of breast cancer. In both cases, the deposited energy by the background γ-ray source is highest. Then, comes the primary neutrons and the background neutrons in that order. Most energy is deposited by the secondary electrons emitted by the particle source interactions. Only the secondary γ-rays (annihilation) and the positrons created by particle interactions occupied in a small part. Since the CdTe detector has a higher probability of absorbing photoelectrons and Z_{eff}, the deposited energy when using the background γ-ray source is higher. When using the primary and background neutron sources, more neutrons are captured, and more characteristic γ-rays are emitted due to the high neutron absorption cross-section of the cadmium atom; then, more secondary particles are created and absorbed [9,29].

The right graph of Fig. 7 shows the energy deposition difference between with and without the sample. Since most primary neutrons are passing through to the sample, their contribution is highest; then the background γ-rays come. The energy deposition contributed by the interaction of the primary neutrons with the sample occupies around 6% (2.47 eV/cm^3). Thus, the primary neutrons contribute much more to the energy deposition compared to background particles. Among these energy deposition values, only the energies of 3.25×10^{-3} eV/cm^3 are deposited by the photoelectric effect at the signal peak of 8.58 MeV. The energy deposition by the background neutrons decreases with the inserted sample because of the screen phenomenon. Some γ-rays emitted from the background neutron capture reactions in the detector are going straight to another detector on the other side without interactions in the current detector. When the sample is inserted, some of these γ-rays are absorbed before reaching the detector on the other side. Thus, the γ-rays interacting with the detector at the other side in the inserted sample decrease compared to those γ-rays without the sample.

Peak area difference at the specific energy between tumor and normal tissues could be a standard for the abnormality of the tissue. The chlorine peaks observed at the energies of 6.12, 7.80, and 8.58 MeV could be used for the detection of abnormality.

The count area ratios for each energy level were calculated using the average peak count area and the standard deviation in the peak

Table 3
The count ratio of signal peaks between tumor and normal tissues of the breast (10^9 particles).

Energy (MeV)	Total Counts for Normal Tissue	Total Counts for Tumor Tissue	Ratio
6.12	2700 ± 152	6500 ± 158	2.41 ± 0.15
7.80	2255 ± 72	3175 ± 77	1.41 ± 0.06
8.58	5563 ± 79	11,669 ± 110	2.10 ± 0.04

count area. As shown in Fig. 6, the peak count areas of the tumor tissue at the specific energies such as 6.12, 7.80, and 8.58 MeV are larger than those of the normal tissue at the same energy levels. Table 3 represents the count ratio of signal peaks between tumor and normal tissues for specific energies – 6.12, 7.80, 8.58 MeV, and each count area ratio is calculated by,

$$Count\ Area\ Ratio = \frac{Total\ Counts\ of\ Tumor\ Tissue\ at\ Specific\ Energy\ Peak}{Total\ Counts\ of\ Normal\ Tissue\ at\ Specific\ Energy\ Peak} \quad (3)$$

The count area ratio could be an indication of the discrimination rate for both tumor and normal tissues. Because the concentration of chlorine in the tumor tissue is almost twice that in the normal tissue, the calculated count ratio should be close to 2. As shown in Table 3, the count area ratios are consistent as approximately 2 in all energy levels.

6. Conclusion

Through this research, the optimized PNF was designed to maximize the production of thermal neutrons. A novel concept for strengthening the sensitivity of the characteristic γ-rays by neutron-material interactions was proposed. Furthermore, this research could be a guideline for the medical application using the PGNAA method by investigating interactions of multiple particles created by neutron-induced.

Due to a relatively high background particle concentration, there was a limitation on using other trace elements except for chlorine. It is difficult to use the other trace elements since their characteristic γ-ray peaks from neutron capture reactions are in the range of lower energy level of the spectrum, which overlapped with backgrounds. Therefore, minimizing the background particles and finding more trace elements, which have large neutron capture cross-sections for high-energy γ-rays, are a top priority for future research. Additionally, this research was processed using only Monte Carlo simulations. The same experiments under the same situations defined this research should be carried out. The sample defined in this research has uniform elemental distribution while the actual tissue has not. In the real experiment, this inhomogeneity could give an effect on the calculation.

Declaration of competing interest

The authors declare that they have no known competing financial interests or personal relationships that could have appeared to influence the work reported in this paper.

References

[1] K. Knapp, Replacement of neutron sources used in well logging by neutron generators, in: 8th PNN & Well Logging Concefence, Eisenstadt, Austria, 2013. Sep. 26 – 27.

[2] J. Reijonen, Compact neutron generators for medical, homeland security and planetary exploration, in: Proc. Particle Accelerator Conference *'05, Knoxville TN, USA*, 2005. May 16 – 20.

[3] R.L. Holm, The uiuc advanced triga and the power reactor community, Trans. Am. Nucl. Soc. 69 (1993) 175–176.

[4] M. Strobl, I. Manke, N. Kardjilov, A. Hilger, M. Dawson, J. Banhart, Advances in neutron radiography and tomography, J. Phys. D Appl. Phys. 42 (24) (2009).

[5] J.R. Lamarsh, A.J. Baratta, Introduction to Nuclear Engineering, Prentice Hall, Upper Saddle River, NJ, 2001.

[6] M. Litz, C. Waits, J. Mullins, Neutron-activated gamma-emission: technology review," Army research Laboratory, Adelphi, MD, Tech. Rep. AFFDL-TR 5871 (2012).

[7] D.B. Pelowitz, Mcnpx user's manual, version 2.7.0, Los Alamos National Laboratory, Los Alamos, 2011. NM, Tech. Rep. LA-CP-11-00438.

[8] B. Ludewigt, Neutron Generators for Spent Fuel Assay, Lawrence Berkeley National Laboratory, Berkeley, CA, 2011. Tech. Rep.

[9] L. Cai, L.J. Meng, Hybrid pixel-waveform CdTe/CZT detector for use in an ultrahigh resolution MRI compatible spect system, Nucl. Instrum. Methods Phys. Res. 702 (2013).

[10] T. Aoki, H. Morii, T. Nakashima, Y. Takahashi, G. Ohashi, Y. Tomita, Y. Neo, H. Mimura, X-ray, gamma-ray detector/imager by CdTe semiconductor and its applications - art. no. 70080R, in: 8th International Conference on Correlation Optics vol. 7008, 2008, p. R80.

[11] V.A. Gnatyuk, T. Aoki, Y. Hatanaka, Laser-induced shock wave stimulated doping of CdTe crystals, Appl. Phys. Lett. 88 (24) (2006).

[12] T. Gandhi, Synthesis and Characterization of CZT Nanowires and its Potential as a Gamma Ray Detector, Ph.D. dissertation, University of Nevada, Reno, NV, 2008.

[13] K. Zanio, Cadmium telluride, in: Semiconductors and Semimetals, Academic Press Inc., New York, NY, 1978.

[14] A. Haghighat, Monte Carlo Methods for Particle Transport, CRC Press, Boca Raton, FL, 2014.

[15] D.S. McGregor, J.T. Lindsay, R.W. Olsen, Thermal neutron detection with cadmium(1-x) zinc(x) telluride semiconductor detectors, Nucl. Instrum. Methods A 381 (2–3) (1996) 498–501.

[16] A.G. Vradii, M.I. Krapivin, L.V. Maslova, O.A. Matveev, A.K. Khusainov, V.K. Shashurin, Possibilities of Recording thermal-neutrons with cadmium telluride detectors, Sov. Atom. Energy 42 (1) (1977) 64–66.

[17] A. Miyake, T. Nishioka, S. Singh, H. Morii, Y. Neo, H. Mimura, T. Aoki, Neutron detection with Gd/CdTe semiconductor detector, in: Hard X-Ray, Gamma-Ray, and Neutron Detector Physics Xii, vol. 7805, 2010.

[18] X5 Monte Carlo Team, MCNP-A General Monte Carlo N-Particle Transport Code, Version 5: Overview and Theory, Los Alamos National Laboratory, Los Alamos, NM, 2003. Tech. Rep. LA-UR-03-1987.

[19] GATE Collaboration Team, Gate user guide version 7.1 [Online]. Available: http://www.opengatecollaboration.org/sites/opengatecollaboration.org/_les/GATE-UsersGuideV7.1.pdf.

[20] R.L. Murray, Nuclear Energy: an Introduction to the Concepts, Systems, and Applications of Nuclear Processes, sixth ed., Butterworth-Heinemann, Burlington, 2009.

[21] W.B.H. Cooke, Predicted Behavior of the AGN 201 Reactor at High Power Levels, Naval Postgraduate School, Monterey, CA, 1961.

[22] M. Mattes, E. Sartori, Jef-1 scattering law data 41, NEA, Paris, France, 1984. Tech. Rep. JEF/DOC, 2.

[23] J.K. Shultis, R.E. Faw, Fundamentals of Nuclear Science and Engineering, CRC Press, New York, 2002. Marcel Dekker.

[24] A.H. Beddoe, S.J. Streat, G.L. Hill, Measurement of total body chlorine by prompt gamma in vivo neutron activation analysis, Phys. Med. Biol. 32 (2) (1987) 191–201.

[25] R.J. Shypailo, K.J. Ellis, In vivo total body chlorine measurements using prompt-gamma neutron activation analysis, J. Rad. Anal. Nuc. Chem. 236 (1998) 19–23.

[26] K.H. Ng, D.A. Bradley, L.M. Looi, Elevated trace element concentrations in malignant breast tissues, Br. J. Radiol. 70 (1997) 375–382.

[27] IAEA, Prompt gamma-ray neutron activation analysis [Online]. Available: https://www-nds.iaea.org/pgaa/pgaa7/index.html.

[28] B.B. Kinsey, G.A. Bartholomew, W.H. Walker, Neutron capture γ-rays from phosphorus, sulfur, chlorine, potassium, and calcium, Phys. Rev. 85 (1952) 1012–1023 [Online]. Available: http://link.aps.org/doi/10.1103/PhysRev.85.1012.

[29] A. Perez-Andujar, L. Pibida, Performance of CdTe, HPGe and NaI(Tl) detectors for radioactivity measurements, Appl. Radiat. Isot. 60 (1) (2004) 41.